Dynamical properties of the figure eight solution of the three–body problem

CARLES SIMÓ

Departament de Matemàtica Aplicada i Anàlisi, Universitat de Barcelona,
Gran Via 585, 08007 Barcelona
E-mail: carles@maia.ub.es

To Don Saari in his 60th birthday

1 Introduction

At the Conference on Celestial Mechanics held in Evanston, A. Chenciner and R. Montgomery gave a proof of the existence of a remarkable periodic solution of the 3–body problem, the *figure eight orbit*, with all the bodies having the same mass and following, with time shift equal to 1/3 of the period, the same path on the plane. This solution lives on the zero level of the angular momentum. See [1, 2, 5] for a description of methods and results, and also [3] for some historical remarks. In fact the solution was displayed for the first time (to my knowledge) by C. Moore [6] as a result of numerical explorations.

The figure eight solution has extremely *remarkable properties*. This paper is devoted to describe some of them. The key property is stability. A part of these results was presented at the above mentioned Conference, as a complement to Chenciner and Montgomery lectures.

The second question we can address is *how exceptional* is the figure eight solution. Are there other choreographies of the 3–body problem letting aside the Lagrange and figure eight solutions? The question, posed like this, was answered in [3]. Indeed, there are satellite choreographies of the eight and relative choreographies (choreographies in a rotating frame) which can give rise to true choreographies in fixed axes (see section 6). These choreographies are a direct consequence of the existence of the eight. We ask for other choreographies in fixed axes, not related to the eight. The answer is positive (see section 7) and, in fact, hundreds of new choreographies of the 3–body problem have been found. They give, definitively, the numerical evidence of the existence of several countable families. Still the figure eight preserves his unique character due to its simplicity and because it is the only one found to be stable.

The paper presents a series of plots summarizing the numerical results. A part of the methods is sketched here. Other methods can be found in [3, 9, 10]. A full account with additional details will be published elsewhere.

2 The eight and nearby simple periodic solutions

To begin with, figure 1 shows the figure eight orbit (top left) as it was initially found, that is, with the initial conditions on the x axis in an Eulerian configuration. As for most of the computations in the paper the total energy has been fixed to $h = -1/2$. The figure eight solution lives on zero angular momentum, $c = 0$. The total mass is equal to 1. Assume the three bodies, of equal mass, are labelled as m_1, m_3, m_2 from left to right. We use the same name to denote the labels of the three masses and the values of the masses. The initial conditions are as follows:

$$E: \ \dot{x}_3 \approx 0.74944\,21910\,77792\,22898\,98659, \quad \dot{y}_3 \approx 1.15017\,89857\,50227\,50240\,30202.$$

Then $\dot{x}_1 = \dot{x}_2 = -\frac{1}{2}\dot{x}_3,\ \dot{y}_1 = \dot{y}_2 = -\frac{1}{2}\dot{y}_3$. The positions (on the x axis) can be recovered from the energy, angular momentum and center of mass integrals as soon as the velocities are know. The period is $T \approx 1.67611\,89237\,59279$. We shall refer to this orbit, when necessary, as orbit E.

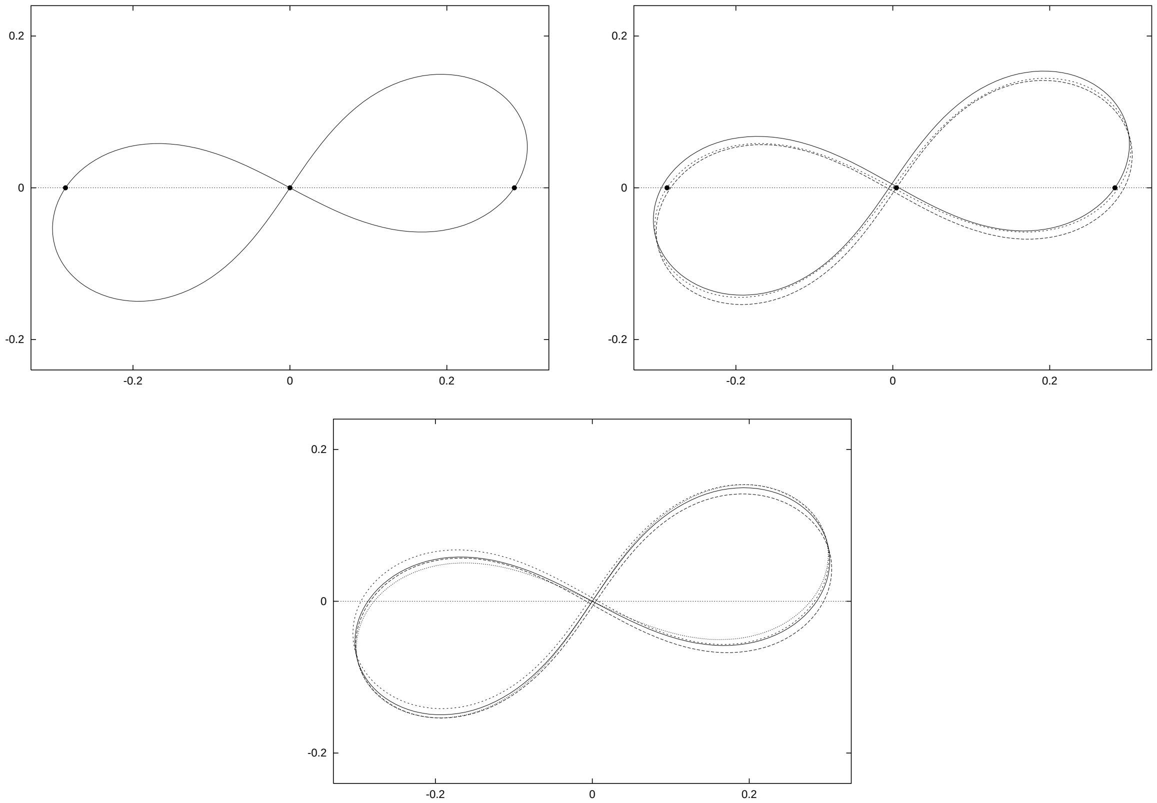

Figure 1: Top left: The figure eight solution with initial conditions in Euler configuration on the x axis. Right: One of the three hyperbolic–elliptic companion orbits. Bottom: The path of one of the bodies in the totally elliptic orbit (solid line) and in the hyperbolic–elliptic orbits (dashed lines). See section 5.

For the computations a systematic use has been made of Taylor series method. Most of the computations have been done in double precision and then the optimal order is usually around 24 (see [11]). Some computations have been done in quadruple precision.

After being suitably rotated, the figure eight solution is symmetric with respect to both the x and y axes. I do not know about the algebraic or transcendent character of the curve. The curve is close to an affine transform of a lemniscate, but the plots can still be distinguished. Taking into account the symmetries, one can try to approximate the curve by algebraic curves of the form

$$f(x,y) = \sum_{k=1}^{m} \sum_{j=0}^{k} c_{2(k-j),2j} x^{2(k-j)} y^{2j} = 0,$$

for different values of m and some normalization (e.g., $c_{2,0} = 1$). Using $m = 2, 3, 4$ the maximal errors are less than $1.3 \times 10^{-4}, 1.7 \times 10^{-7}$ and 5×10^{-9}, respectively. Even with $m = 2$ one cannot distinguish the eight from $f(x,y) = 0$ without magnification.

Three additional periodic orbits have been found near the figure eight, keeping all the masses equal. In these solutions the three bodies move on different figure eight curves. These orbits will be labelled H1, H2 and H3. Initial conditions for them are

$$
\begin{array}{llcl llcl}
H1: & \dot{x}_{3,H1} & \approx & 0.75881\,62806\,68459\,, & & \dot{y}_{3,H1} & \approx & 1.14793\,42585\,54521\,, \\
 & \dot{x}_{2,H1} & \approx & -0.40009\,31630\,24594\,, & & \dot{y}_{2,H1} & \approx & -0.58791\,53123\,82955\,, \\
H2: & \dot{x}_{3,H2} & = & \dot{x}_{3,H1}\,, & & \dot{y}_{3,H2} & = & \dot{y}_{3,H1}\,, \\
 & \dot{x}_{2,H2} & = & \dot{x}_{1,H1}\,, & & \dot{y}_{2,H2} & = & \dot{y}_{1,H1}\,, \\
H3: & \dot{x}_{3,H3} & \approx & 0.73143\,93556\,99436\,, & & \dot{y}_{3,H3} & \approx & 1.15550\,45090\,33398\,, \\
 & \dot{x}_{2,H3} & = & -\frac{1}{2}\dot{x}_{3,H3}\,, & & \dot{y}_{2,H3} & = & -\frac{1}{2}\dot{y}_{3,H3}\,,
\end{array}
$$

the positions (again on $y = 0$) being recovered as before. We observe that H1 and H2 are symmetric the one from the other just permuting bodies m_1 and m_2. On the other hand H3 shares with E the conditions $\dot{x}_2 = -\frac{1}{2}\dot{x}_3$, $\dot{y}_2 = \frac{1}{2}\dot{y}_3$. For the three H orbits the period is the same, $T \approx 1.67611\,91959\,47797$. In fact the three orbits are obtained from one of them by suitable rotations. Indeed, using a transversal section $\mathcal{C}$ (see next section), the three H orbits and the E orbit are fixed points of the sixth power of the return map to this section. In suitable normal form coordinates, the three H points are at the vertices of an equilateral triangle having the center at E.

3 Scanning a 2D subsection. A sample of orbits

The planar 3–body problem is a 4 degrees of freedom (DOF) system. By fixing the angular momentum ($c = 0$ for the moment being), it is reduced to 3 DOF. On a vicinity of the periodic orbits above, we can use the passage through collinear configuration as a suitable transversal section, $\mathcal{C}$. The E and H orbits of section 2 pass 6 times through $\mathcal{C}$ before closing.

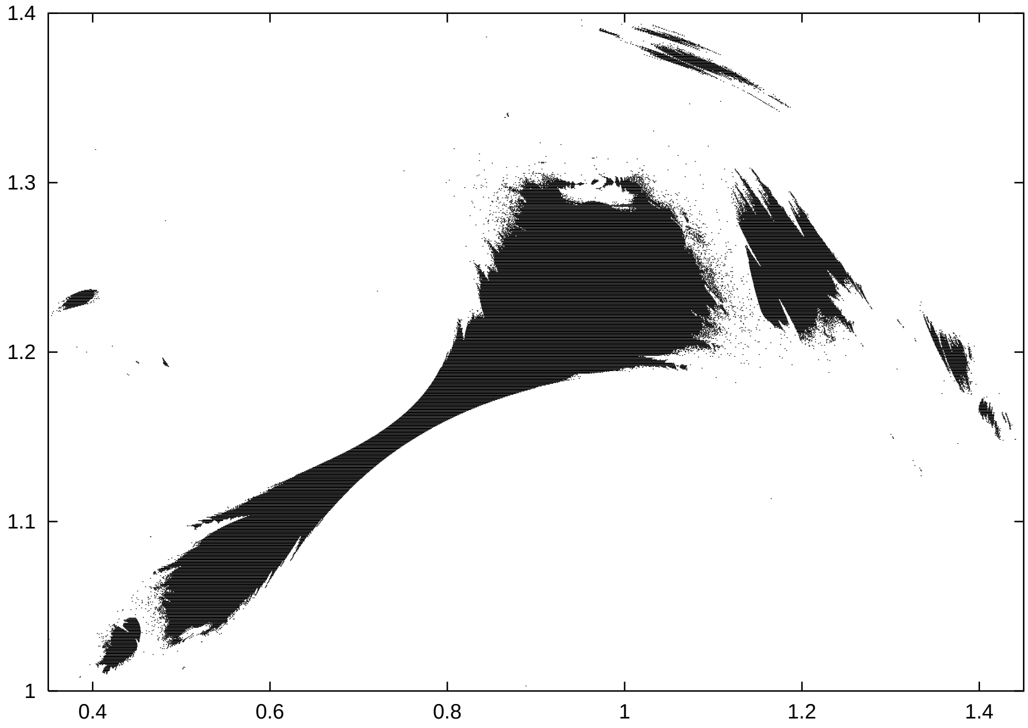

Figure 2: Top: The main zone of stability.

Given $\dot{x}_2$, $\dot{y}_2$, $\dot{x}_3$, $\dot{y}_3$ together with $h = -1/2$, $c = 0$ is enough to determine initial conditions in $\mathcal{C}$ (even if the masses are not equal). In this 4D manifold it is natural to take a 2D subsection,

$\mathcal{C}_2$ defined by $\dot{x}_2 = -\frac{1}{2}\dot{x}_3,\ \dot{y}_2 = \frac{1}{2}\dot{y}_3$, to scan for possible interesting orbits. In $\mathcal{C}_2$ a point is identified by $(\dot{x}_3, \dot{y}_3)$.

The scanning rule has been:

- Take some initial point on $\mathcal{C}_2$ and compute up to a maximum of 30 000 passages through $\mathcal{C}$ (say, 5 000 full "revolutions" for data close enough to E, see section 5).
- Stop the computations in case a passage too close to collision is produced ($\min_{1\le i<j\le 3}\{r_{i,j}\} < 10^{-6}$) or the maximum of the distance is too large (say > 10). Typically, a close approach is produced before the bodies escape. Here $r_{i,j}$ means, of course, the distance from m_i to m_j.
- Plot the initial conditions of the points in $\mathcal{C}_2$ which subsist without "escaping" until the end of the computation.

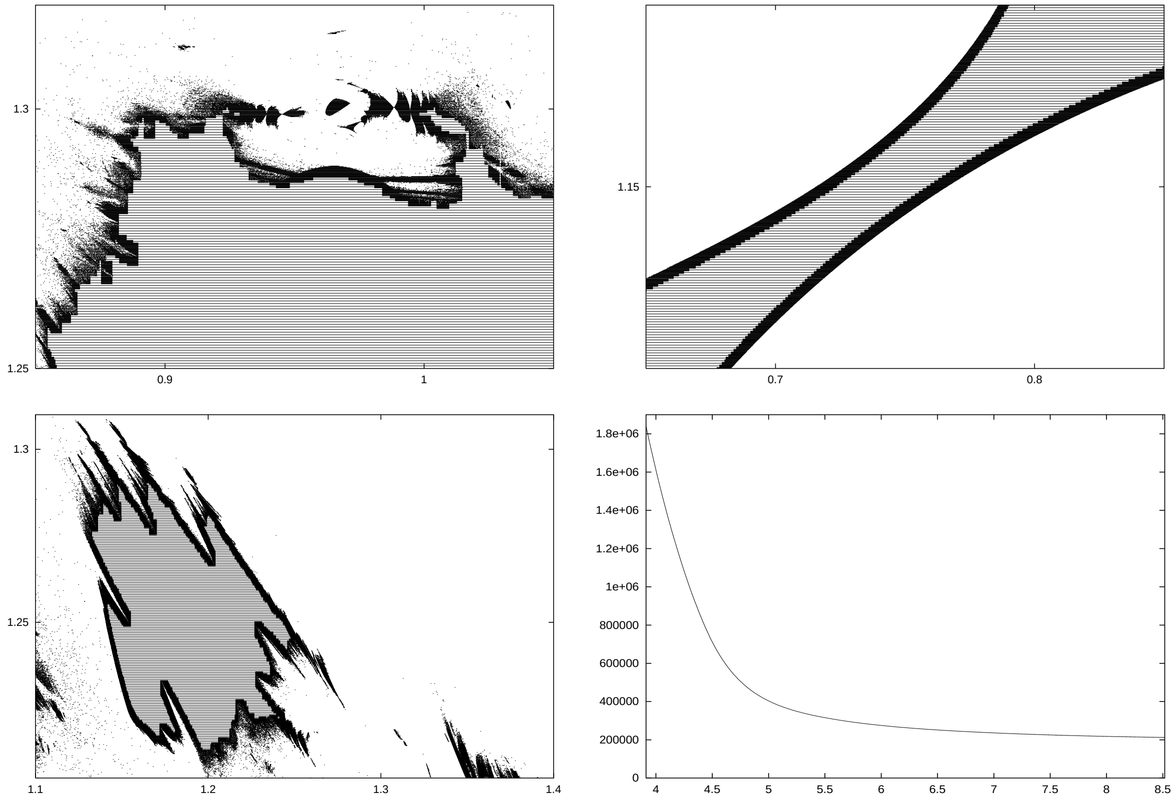

Figure 3: Details of different parts of the main stability zone of figure 2. Bottom right: Evolution of the number of points not escaping in the scanning as a function of the number of full revolutions. The horizontal scale is logarithmic in the range $[50, 5000]$.

The results of that test are shown in figure 2. Initially the data are taken on a grid, between 0.0005 and 3 with step size 0.0005 both in the $\dot{x}_3$ and $\dot{y}_3$ components. It is worth to mention that the point E is close to the center of the narrow region which is seen at the center of the figure (see figures 4,7 for a more clear identification). The part of the plot between the E point and the left lower corner seems to be symmetric (with some deformation, from the part towards the right upper direction. Beyond the main region seen in figure 2 one can see several other small regions of "stability". Some tiny regions have been also detected for smaller values of $\dot{y}_3$. Close to the center of these small "stability islands" periodic orbits with complicated patterns have been found, even having relatively close approaches to collision. They seem to be stable, as seems to be the E orbit. See section 5 in what concerns the E orbit. However orbit E is the only one found in this scanning which gives rise to a choreography.

Some remarkable facts of the main zone of stability are the following:

- We started scanning 36×10^6 initial data. Most of them escape very soon. After 300 (resp. 3 000) passages through $\mathcal{C}$ the number of orbits which subsist is near 1.84×10^6 (resp. 2.63×10^5). For 30 000 passages through $\mathcal{C}$ still more than 2.12×10^5 points subsist. Figure 3 bottom right shows the evolution of the subsisting points as a function of the number of full revolutions. This gives an indication on the existence of orbits which subsists forever. Longer runs have been conducted on selected pieces which show that the decay is quite slow from that point on.
- Another series of runs has been done near the boundaries of the previously obtained zone and with step size 10^{-4}. Some results are shown in figure 3 top and bottom left. It is interesting to observe the difference of behavior in different zones. On the left plots there are domains with a well defined boundary, but still some amount of scattered points which can be predicted to escape under further iteration.
- An opposite behavior appears on the top right plot, close to the location of E. The boundary is very sharp. In fact, there are no essential changes on it after a few initial iterates. This suggest that most of the points inside this part of the picture should subsist forever and that only a tiny fraction is affected by diffusion.

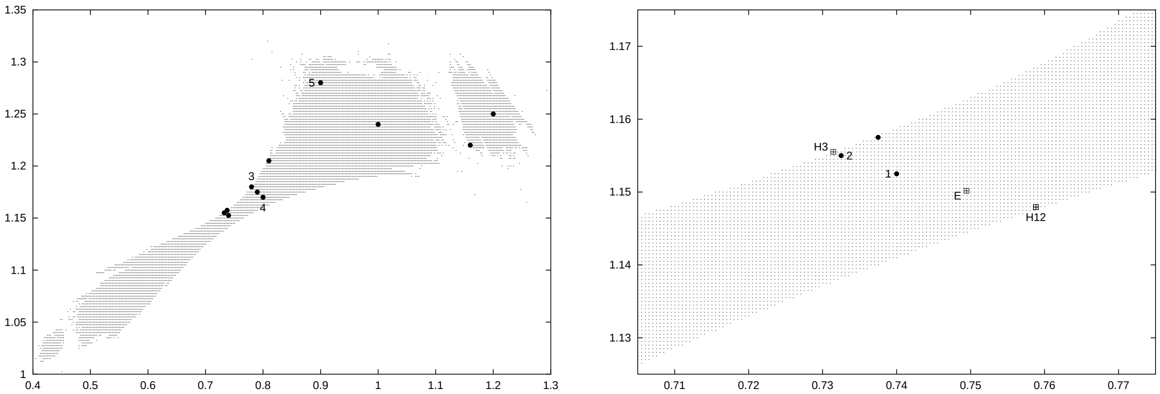

Figure 4: Magnifications of figure 2 showing the location of the initial conditions for the periodic orbits and for the tori displayed in figures 5 and 6.

To have an idea of the behavior of non-escaping orbits close to the figure eight, we have taken several initial conditions in $\mathcal{C}_2$ and produced iterates of the full Poincaré map, that is, after 6 passages through $\mathcal{C}$. A sample of initial conditions is shown in figure 4. For the reader's convenience the location of E and H3 is also shown, as well as the projection of H1 and H2 on $\mathcal{C}_2$. Note that the H points seem to be related to the sharp boundaries of the stability domain near E. Other marked unnumbered points in figure 4 display also nice properties but are not included here.

For checking purposes we give here the data in $\mathcal{C}_2$ for the numbered points in figure 4.

$$
\begin{array}{lllll}
\text{Data 1:} & \dot{x}_3 = 0.74, & \dot{y}_3 = 1.1525, & 10\,000 & \text{iterates,} \\
\text{Data 2:} & \dot{x}_3 = 0.7325, & \dot{y}_3 = 1.155, & 10\,000 & \text{iterates,} \\
\text{Data 3:} & \dot{x}_3 = 0.78, & \dot{y}_3 = 1.18, & 20\,000 & \text{iterates,} \\
\text{Data 4:} & \dot{x}_3 = 0.8, & \dot{y}_3 = 1.17, & 10\,000 & \text{iterates,} \\
\text{Data 5:} & \dot{x}_3 = 0.9, & \dot{y}_3 = 1.28, & 30\,000 & \text{iterates.}
\end{array}
$$

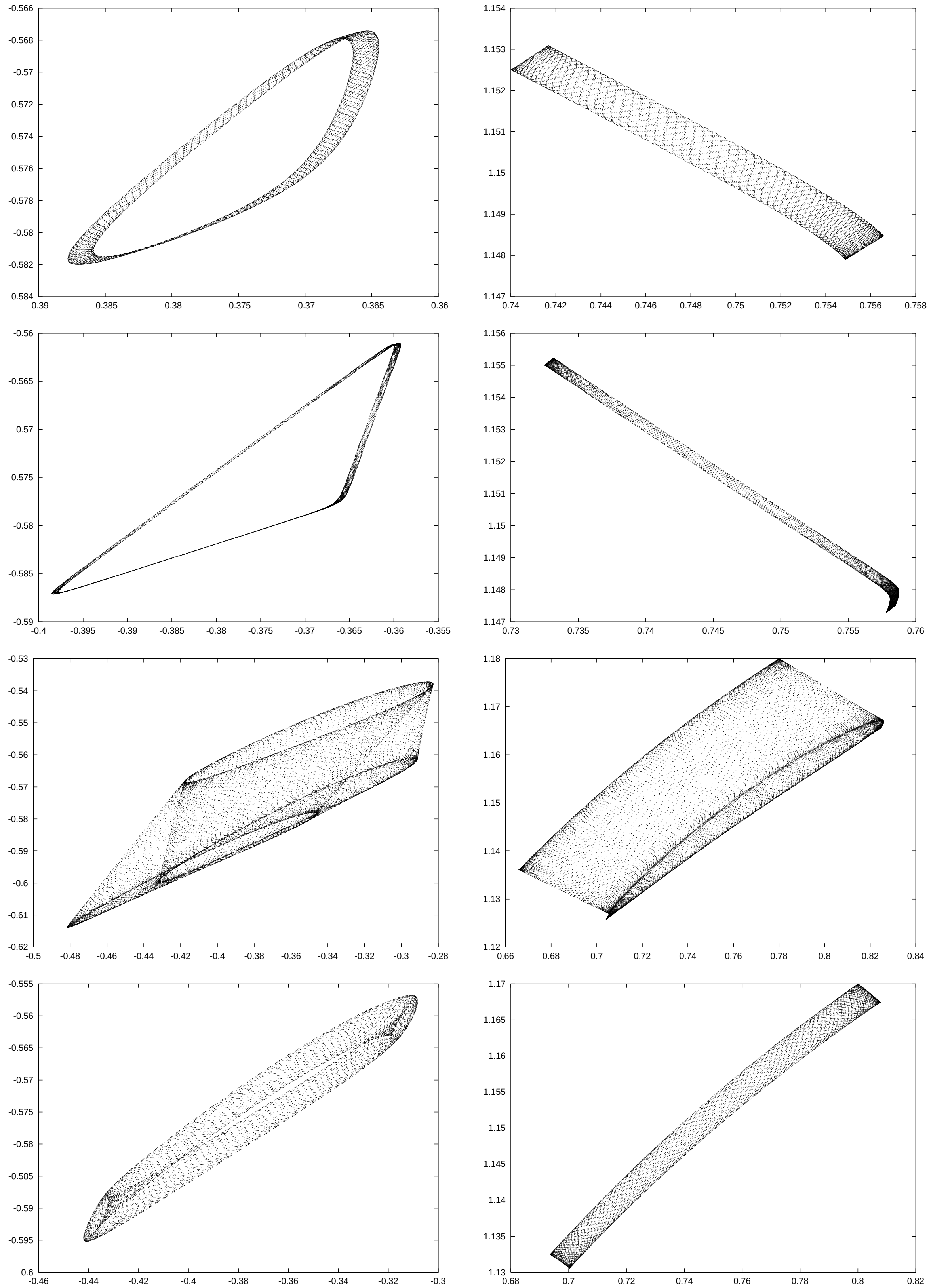

Figure 5: A sample of tori not far from the figure eight solution. From top to bottom correspond to initial conditions identified by points numbers 1 to 4 in figure 4. Left: projections of the points in $\mathcal{C}$ on the $(\dot{x}_2, \dot{y}_2)$ variables. Right: Idem on the $(\dot{x}_3, \dot{y}_3)$ variables.

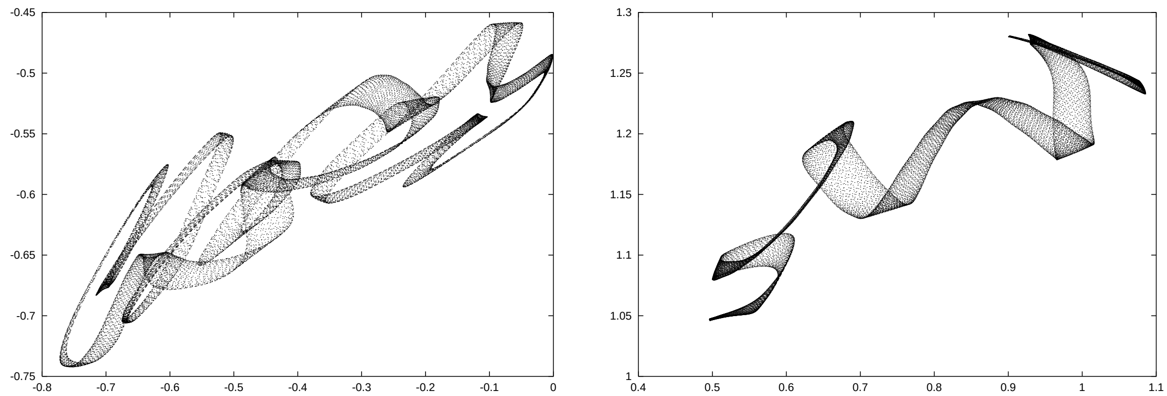

Figure 6: Same as figure 5 for the fun torus corresponding to number 5 in figure 4.

For each of these data, projections of the corresponding 2D tori on $\mathcal{C}$ are displayed in figures 5 and 6. They give 3D tori in the phase space, confined to $c = 0$. See comments of the shapes of these tori below in this section.

On the other hand it is also natural to look for 2D tori in the phase space, to be seen as invariant curves in $\mathcal{C}$. There are two main (Cantorian) families emanating from the point E (see section 4). Beyond these families one can find the families associated to simple resonances between the components of the rotation vector of the 2D tori. At least if the resonances are not of a too high order.

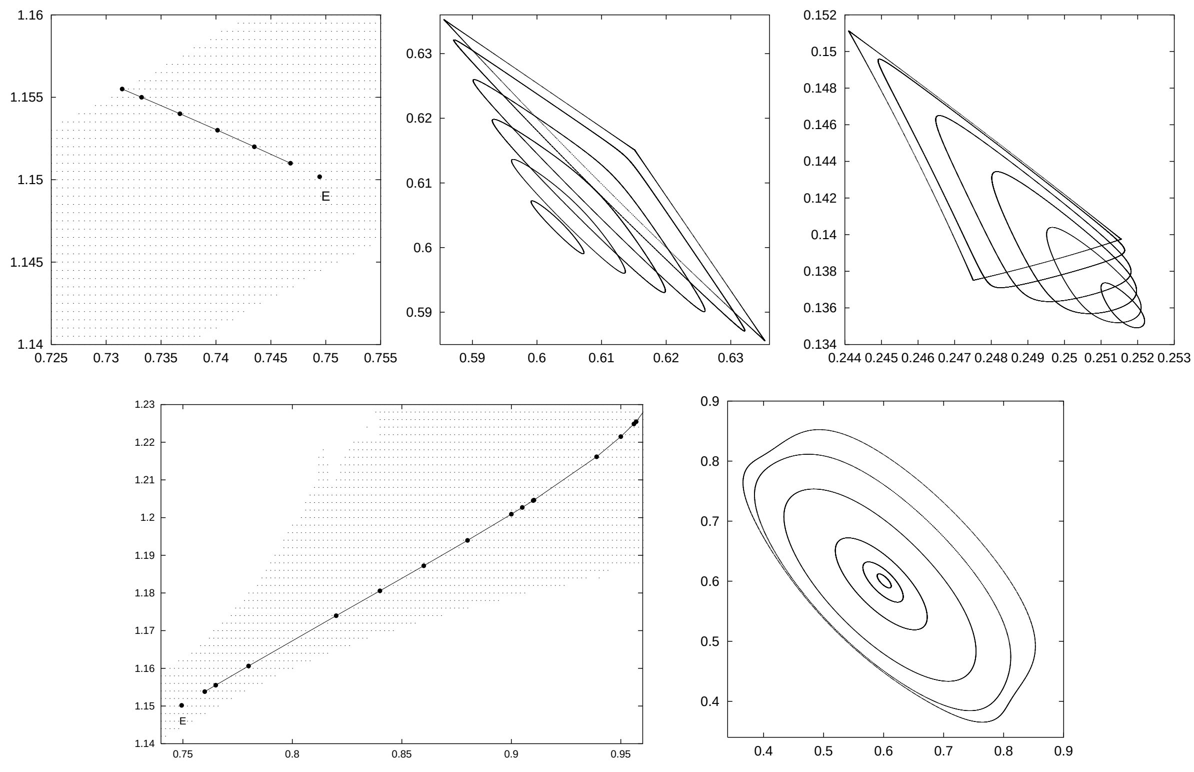

Figure 7: Top: On the left the characteristic curve of the slow mode family of invariant curves of the Poincaré map. The middle and right plots show two projections of these curves. Bottom: On the left the characteristic curve of the fast mode family of invariant curves. On the right a projection of these curves. See the text for additional explanations.

For that purpose different methods have been used. One of them is the synthesis of a return map (see, e.g., [8]). Another simple method consists in computing 2D tori, doing a frequency analysis to determine the basic frequencies and related amplitudes of the fundamental harmonics and using then a zero finding method to turn to zero the amplitude of the undesired frequency. A sample of results is shown in figure 7.

To identify each one of the 2D tori it is enough to give initial conditions (i.e., one point in $\mathcal{C}_2$) or the (resonant) frequencies or whichever conditions allow to recover a torus. The locus of these data for a one–parameter family is named “characteristic curve”. Sometimes one uses loosely the name characteristic curve for something which is, in fact, some projection of the characteristic curve. This is completely similar to what is usually done to represent families of periodic orbits.

The left plots show details of the stability zone of figure 2 with the location of the characteristic curves of the two main families of 1D tori, together with the location of E, in $\mathcal{C}_2$. On the top row the family corresponds to the *slow frequency* (see section 4). Note that the characteristic of the slow family goes, essentially, from E to the H3 point. The center and right plots show projections on $(\dot{x}_2, \dot{x}_3)$ and (x_2, y_2), respectively, of a selected set of invariant curves, corresponding to the marked points on the left. Note that when we progress along to family, from E to the boundary, the size of the curves increases and the shape tends to a triangle. In fact the 2D torus of the phase space spanned by this triangle approaches the three H periodic orbits described before. Furthermore, the rotation number of the dynamics restricted to the invariant curve, which was already small at E, tends to zero when we approach the boundary.

The bottom of figure 7 corresponds to the *fast mode*. The rotation number is not small at E (see section 4) and is slowly decreasing when going away from E, while the invariant curves, shown in the right part, increase size.

Note that the “characteristic curves” shown in figure 7 are, in fact, Cantorian sets. However, the gaps are too small to be seen with this resolution. We have chosen not to mark the points on these curves close to E, but really this is the part of the “curve” where the Cantor set is more “fat” (the complement of the Cantor has a relative measure exponentially small with respect to the distance to E).

We have that close to the central region of the domain of stability, around E, the two main modes are, essentially, curves which tend to have a triangular shape and an elliptic shape, respectively. If we compare with the tori shown in figure 5, we see that the system is close to a product, and not too far from integrable. Tori numbers 1 and 4 in figure 5 are not too far from invariant curves of slow and fast modes. The complementary amplitude is small. Torus number 2 is very close to a triangular shape invariant curve, while torus number 3 is close to the product of a triangle by an ellipse, as corresponds to a point close to the boundary and not too close to the slow family characteristic curve.

4 Study of the local behavior

The key feature of the figure eight solution is *stability*. First of all the eigenvalues of the Poincaré map on $\mathcal{C}$, restricted to $c = 0$, can be computed. They are equal to $\lambda = \exp(\pm 2\pi i \nu_j)$, $j = 1, 2$. The numerical values $\nu_1 \approx 0.00842\,27247\,08131$ and $\nu_2 \approx 0.29809\,25290\,04750$ have been found. The small value ν_1 is related to the slow mode and ν_2 to the fast mode. This ensures linear stability.

To obtain information on the nonlinear properties we need to represent the Poincaré map around the fixed point by power series. We know that the map is analytic, due to the analyticity of the vector field away from collisions. One possible way to obtain this information is by integration of higher order variational equations. See [7] for the formulation and examples. Here we have used successfully a different approach: Numerical differentiation.

It is well known that for a function $F(X)$, $X \in \mathbb{R}^n$, the components of $D^kF(X)$ can be approximated as a linear combination with suitable weights of the values of F at points of a grid around X with spacing ε (see, e.g. [12]). There is no need to have the same spacing in all the n coordinates, but we shall assume this for simplicity. Let $\mathcal{D}^kF(X,\varepsilon)$ the values obtained in this approximation. For practical purposes we note that all the components of $\mathcal{D}^kF(X,\varepsilon)$ are computed using the same grid and that only the points in the grid that are really needed are computed.

If F is of class $\mathcal{C}^{k+2}$ then for a fixed X the error has the form

$$\mathcal{E}(\varepsilon) := ||\mathcal{D}^kF(X,\varepsilon) - D^kF(X)|| \approx A\varepsilon^2 + B/\varepsilon^k,$$

if we choose to use numerical differentiation formulas with truncation order of second order in ε. Here A and B are related to bounds of $||D^{k+2}F||$ on a neighborhood of X and to the errors produced in the computation of the values of F on the used grid. It is clear that they depend on k. These values can be estimated if grids with different values of ε are used.

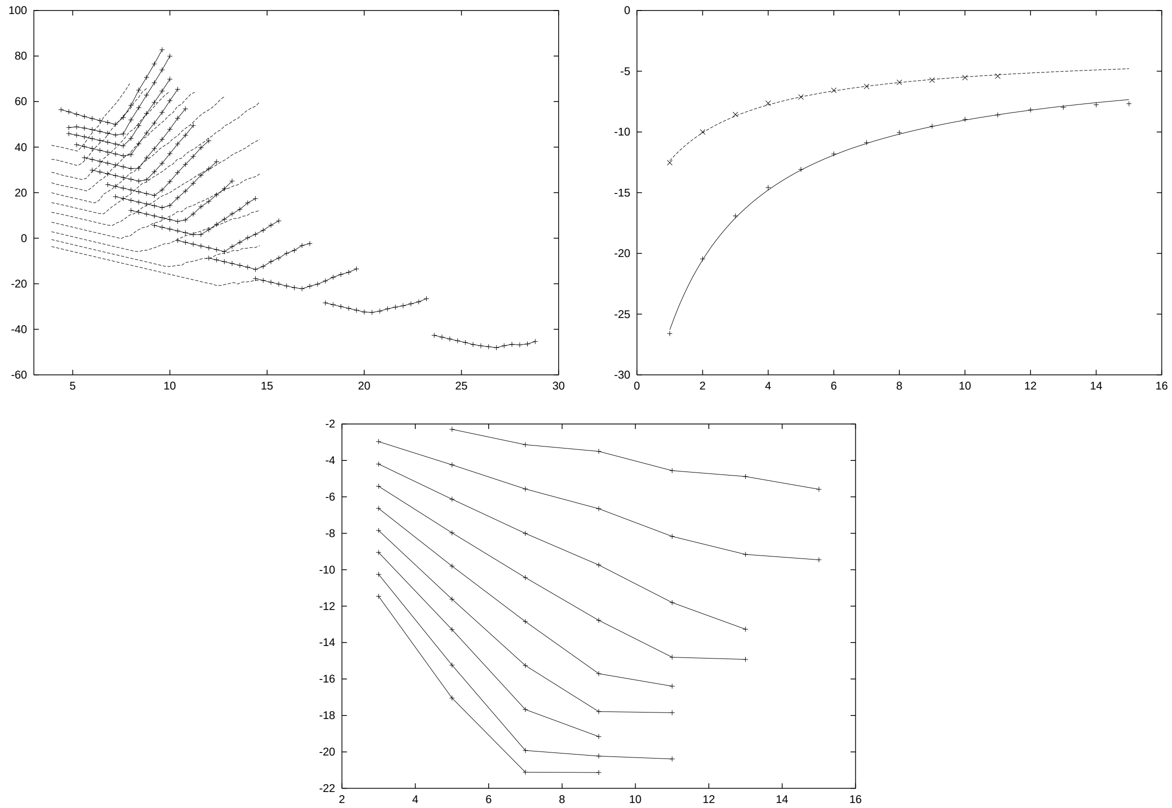

Figure 8: Top: On the left the behavior of the estimates of the error in the numerical differentiation, as a function of k and ε. On the right the behavior of the optimal step size as a function of the order. Bottom: Bounds of the model errors as a function of the order in different domains. See text for detailed explanations.

This procedure has been implemented automatically in the present problem. The variable X consists of the parameters in $\mathcal{C}$: $(\dot{x}_2, \dot{y}_2, \dot{x}_3, \dot{y}_3)$. According to what has been said, we can compare $\mathcal{E}(\varepsilon_1)$ with $\mathcal{E}(\varepsilon_2)$ using $\varepsilon_2 = \gamma\varepsilon_1, \gamma \in (\gamma_0, \gamma_1)$, $0 < \gamma_0 < \gamma_1 < 1$, for a sequence of values of ε_1. As a representation of these differences, $\Delta\mathcal{E}(\varepsilon_1)$, we use the maximum of the values obtained for all the components of $\mathcal{D}^kF(X,\varepsilon_1) - \mathcal{D}^kF(X,\varepsilon_2)$. We should obtain a result of the form

$$\Delta\mathcal{E}(\varepsilon_1) \approx \hat{A}\varepsilon^2 + \hat{B}/\varepsilon^k,$$

where $\hat{A}$ and $\hat{B}$ differ of A and B by constant factors depending on γ.

Figure 8 top left shows the results using as X the point corresponding to the figure eight solution and the Poincaré map as F. In the figure we plot the estimated value of $\log|\Delta\mathcal{E}(\varepsilon)|$ versus $|\log\varepsilon|$. For small ε the dominant behavior has slope k, while for large ε it should be -2. In figure 8 the solid line and the crosses display the results in quadruple precision and for $k = 1, \ldots, 15$, while the dashed lines correspond to double precision and $k = 1, \ldots, 11$. One can check that the agreement with the predicted behavior is excellent.

The best estimates of the components of $D^kF(X)$ are obtained for the values of ε such that $|\Delta\mathcal{E}(\varepsilon)|$ is minimum. It is clear that for different k optimality corresponds to different values of ε. Let ε_k be the optimal value for order k. Assuming analyticity (as in the present case) and that the largest coefficient of order k of the Taylor series behaves like cd^k for some positive constants c and d, it is immediate to derive the formula

$$\log\varepsilon_k \approx \alpha + \frac{\beta}{k+2},$$

where α, β are positive constants. This behavior is checked in figure 8 top right. This is quite interesting, because it allows to have good predictions of ε_k, so that only a few values of ε have to be tested for each k. The plots here use too many values of ε only for illustrative purposes.

With the approximated coefficients of the Taylor representation of the Poincaré up to some order k, we have a simple analytic model. We can produce estimates of the errors between the model around E and the direct use of Poincaré map. These errors can be estimated on a grid on the sphere of radius ρ in $\mathcal{C}$. The results are shown in figure 8 bottom. We plot $\log_{10}$(maximal error) as a function of k for $\rho = 0.001 \times 2^j$, $j = -2, \ldots, 6$. The different values of ρ correspond to the different lines from bottom to top. The results given in the plot have been obtained using quadruple precision, but they are not too different (except for ρ very small) if they are produced in double precision.

It is worth to mention that the errors concerning the image under the model for the three fixed points H1, H2 and H3 are below 10^{-12} using order 9. No further improvement occurs for higher orders. Even for $\rho = 0.06$ it is possible to achieve errors of the order of 10^{-6}.

This has two relevant consequences:

- Having the model at hand, it is a routine task to obtain a normal form. The fact that the coordinates used are non symplectic, is irrelevant. In particular the model at order 3 gives that the *torsion is non degenerate*. Hence, one can apply the KAM theorem, which ensures that most of the tori "seen" in the model *do really exist*.

- The goodness of the model in a neighborhood which includes the E point and the three H points allows to construct a *semi-global model*, that is, a model valid on a relatively large domain. In particular the stability properties of the H points can be checked from this model. One recovers, approximately, the traces. That is the values $tr_1 = \lambda_1 + \lambda_1^{-1}$, $tr_2 = \lambda_2 + \lambda_2^{-1}$, where λ_1, λ_1^{-1}, $\lambda_2, \lambda_2^{-1}$ are the eigenvalues of the differential of the Poincaré map evaluated in the points H. A direct computation of them gives the values

$$tr_1 \approx 2.00838\,77350\,62189, \quad tr_2 \approx -0.58895\,54022\,02053.$$

From these values it is clear that the H points are of hyperbolic–elliptic type. The eigenvalues $\lambda_1 \approx 1.09587\,44193\,78570$, $\lambda_2 = \exp(2\pi i\nu_3)$, $\nu_3 \approx 0.29757\,28352\,61762$, follow.

We can consider the behavior of the Poincaré map on a vicinity of E as having 4 fixed points: three at the vertices of a triangle, the other at the center. These points are close to a 2D submanifold. On the complementary directions one has, essentially, a twist map. The Poincaré map is close to a product, as already mentioned. Note, also, that the 1D invariant manifolds of the H points almost "match" by homoclinic connections. The distance between these manifolds is exponentially small in the distance between the points, which is small in the present case. This is what justifies the sharpness of the boundary seen in figure 3 top right. Points inside the product of the "triangle" by a disc remain confined (except by Arnol'd diffusion and by the small lack of coincidence of the manifolds, both of them exponentially small phenomena). On the other hand, starting outside the triangle leads to quick escape.

The boundaries of the stability domain near E are the stable/unstable manifolds of the center manifold of the H points. When we proceed along the boundary going away from E the lack of coincidence of the manifolds becomes more relevant, as seen in figure 2. This seems to be a reasonable explanation to the observed behavior.

5 Stability as a function of the masses and related bifurcations

In this section we shall also consider the masses as variables, but keeping again $h = -1/2$, $c = 0$ for energy and angular momentum. We use $\mathcal{C}$ as suitable section. We are interested in the evolution of the periodic orbits as a function of the masses and, mainly, in the stability properties. The periodic orbits will no longer be choreographies when the masses change.

We shall represent the masses as the barycentric coordinates in an equilateral triangle with vertices at $(0,0)$, $(1,0)$, $(1/2, \sqrt{3}/2)$. The coordinates of a point of the triangle are represented as (μ, ν). The values $(\mu_0, \nu_0) = (1/2, \sqrt{3}/6)$ correspond to equal masses, a point in the mass space that we shall represent as M. Given (μ, ν) we have $m_3 = 2\nu/\sqrt{3}$, $m_2 = \mu - m_3/2$, $m_1 = 1 - m_2 - m_3$.

Locally near M there exist also 4 periodic orbits and they have the same character as for M. As we shall see, we should restrict to a very small domain around M if we are interested in having stable orbits. Hence, one of the eigenvalues remains always elliptic (the fast mode). We shall concentrate on the behavior of the other one. When we refer to a trace we mean the trace associated to this mode.

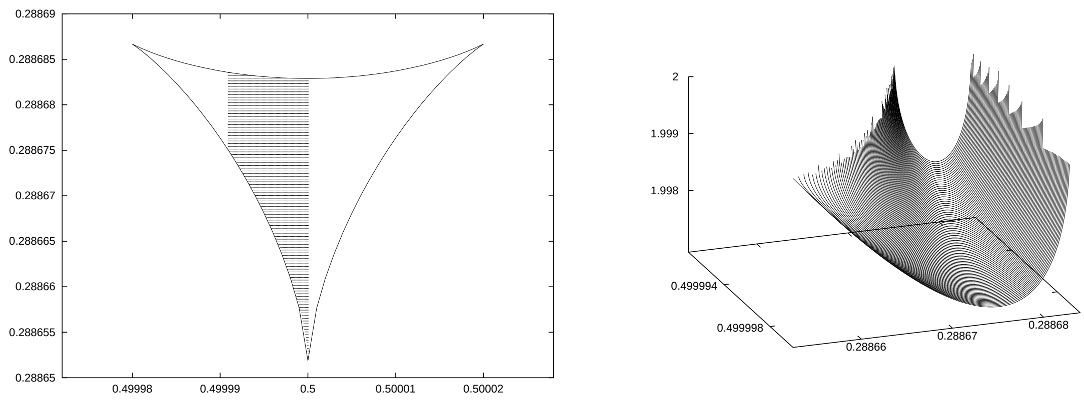

Figure 9: Left: The domain on the mass triangle where the p.o. is stable. Right: A plot of the trace close to 2 as a function of the masses, for a part of the triangle. The projection of this part is also shown on the left.

Figure 9 left shows the domain of the mass triangle near M where the orbit obtained by evolution of E is totally elliptic. The other three orbits still exist in that domain and are hyperbolic–elliptic. Due to the symmetry in the mass space it is enough to discuss what happens in 1/6 of the triangle. However, for a better illustration we consider a strip on the triangle covering almost 1/2 of the total and the periodic orbits and related trace have been computed on it. The right part of the figure shows the trace on the strip. It is clear that approaching the leftmost vertex of the triangle the trace goes to 2. Going to this vertex along $m_1 = m_3$ we have the same behavior as in the front line of the right plot.

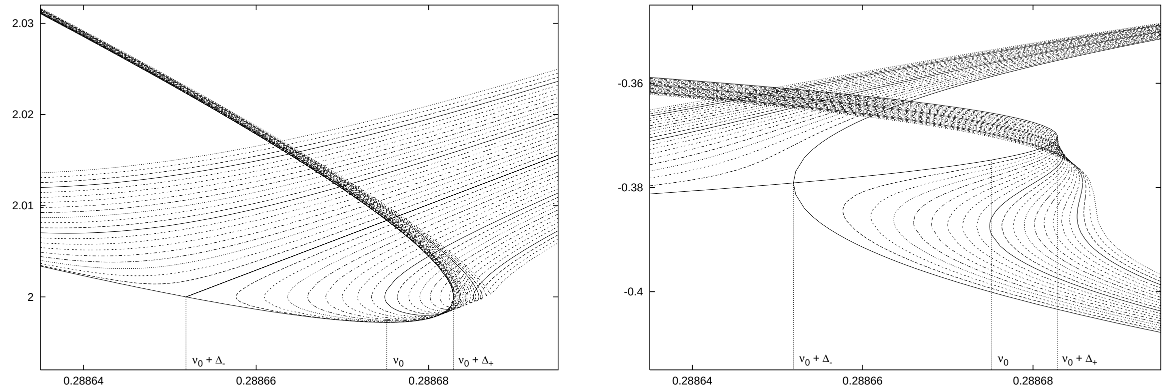

Figure 10: Left: Projections of traces vs ν for values of μ in $[0.499979, 0.5]$ with step 10^{-6}. Right: Similar projections of $\dot{x}_2$ vs ν. Note that two different arcs on the right project on the same line on the left.

The first thing to note is that the triangle is very small. On the line $\mu = 1/2$ ($m_1 = m_2$) the lower vertex differs from the center of the triangle by $\Delta\nu_- = -2.32 \times 10^{-5}$. The central point of the upper side has $\Delta\nu_+ = 0.77 \times 10^{-5}$. This means that the minimum and maximum values of the masses in the triangle are ≈ 0.33330654 and ≈ 0.33334673, respectively.

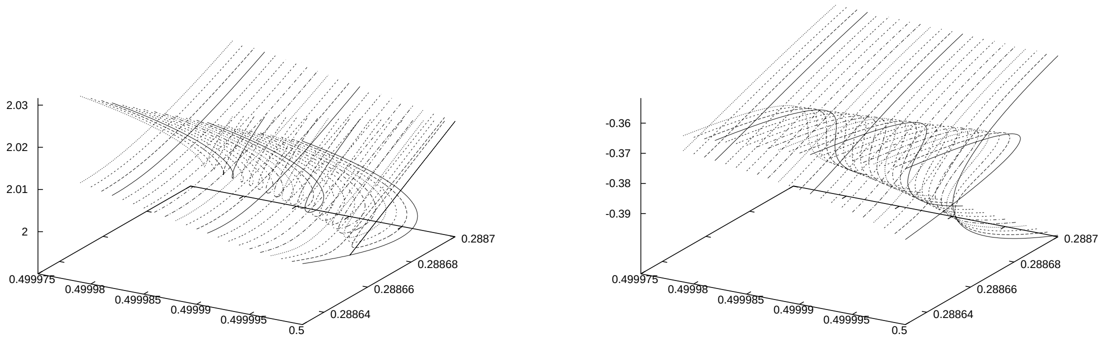

Figure 11: 3D views of figure 10.

Along the boundary of the triangle an elliptic-hyperbolic bifurcation is produced, the hyperbolic orbit being different on each side of the triangle. For a better understanding of the bifurcations, figure 10 plots the traces of all the orbits obtained by evolution of E and the H, on different slices $\mu =$ ctant. The solid line seen on the lower part of figure 10 left, corresponds to $\mu = 1/2$, folds at $\nu = \nu_0 + \Delta\nu_+$ and goes up near the upper left corner. At the point on the lower part with $\nu = \nu_0 + \Delta\nu_-$ (i.e., the vertex of the triangle) another bifurcation is produced. It is a pitchfork bifurcation. Going from left to right along the curve in the plot we pass from a hyperbolic orbit to an elliptic one plus two hyperbolic orbits. In this plot both new hyperbolic orbits have the same projection. Check the right part of figure 10 for a different projection to see this.

When μ goes away from $1/2$ the corresponding curves on figure 10 left have either no bifurcation or two elliptic-hyperbolic bifurcations. There exist always (at least not too far from M) two hyperbolic p.o. obtained by evolution of what exists at M, and four solutions exist only inside the triangle. Figure 11 shows a 3D view of the trace as a function of (μ, ν) (on the left) and of $(\dot{x}_2, \nu)$ (on the right).

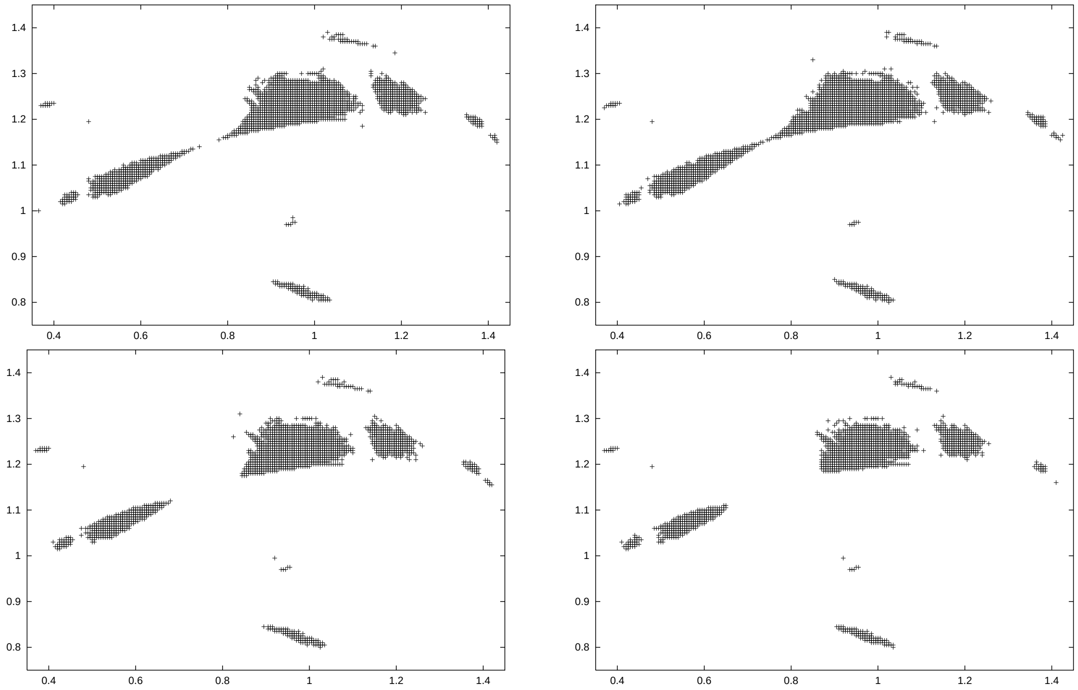

Figure 12: Stability domains for nearby masses. see the text for the used masses.

What is the effect of mass variations on the stability domains similar to the one displayed in figure 2? We have seen that the domain of stability is relatively large for equal masses. Of course, when the totally elliptic orbit is absent (outside the triangle of figure 9) all stable objects that we had close enough to E should disappear. The effect of moderate variations of (μ, ν) is quite dramatic. If the variations are very small (of the order of a small multiple of 10^{-5}) some decrease of the stability domain is already present. Figure 12 shows some cases. Top left corresponds to $m_1 = m_2$, at the pitchfork bifurcation. Top right to $m_1 = m_2$, at the elliptic–hyperbolic bifurcation. The parameter variations with respect to equal masses on the left and right bottom plots are $(\Delta\mu, \Delta\nu) = (-1, -4) \times 10^{-5}$ and $(-3, -5) \times 10^{-5}$, respectively.

Just to keep some data: using a very rough grid with step 0.005 in both directions in the range $[0, 2]$ the number of points which subsist for 5 000 full Poincaré iterates is (from left to right and from top to bottom) 1 741, 1 991, 1 545 and 1 338, respectively. Note that these values are not far from 1% of the points in figure 2, where a grid of step 0.0005 was used.

Restricting the attention to $\mu = 0.5$, the data decrease slightly for $\Delta\nu = \pm 10^{-4}$, for which the number of subsisting points is around 1 000. They are a few hundreds when $\Delta\nu$ is around $\pm 10^{-3}$, and essentially no point subsist for $|\Delta\nu|$ of the order of 10^{-2}.

6 Satellite and relative choreographies

We return to equal masses for the rest of the paper.

We summarize here some results presented in [3] about choreographies related to the eight. I refer to that paper for further details. As already mentioned the figure eight solution is totally elliptic. Locally it is close to the product of two twist maps with a small coupling. We can select suitable amplitudes so that we have periodic orbits in each one of the maps. To prevent from too large periods, we select the amplitude of the slow mode equal to zero. Hence, we are moving on the characteristic curve of the fast mode (see figure 7 bottom left). If the rotation number is rational, we shall have a periodic orbit. We can call it a *satellite* of the eight.

Not all periodic orbits of the Poincaré map give rise to a choreography. If we restrict to the fast mode characteristic, the rotation number must be of the form p/q with $(q, 3) \neq 0$. Figure 13 left shows an example of satellite choreography with rotation number $11/37$. For reference the eight is also shown. The dots correspond to initial conditions at some arbitrary initial time.

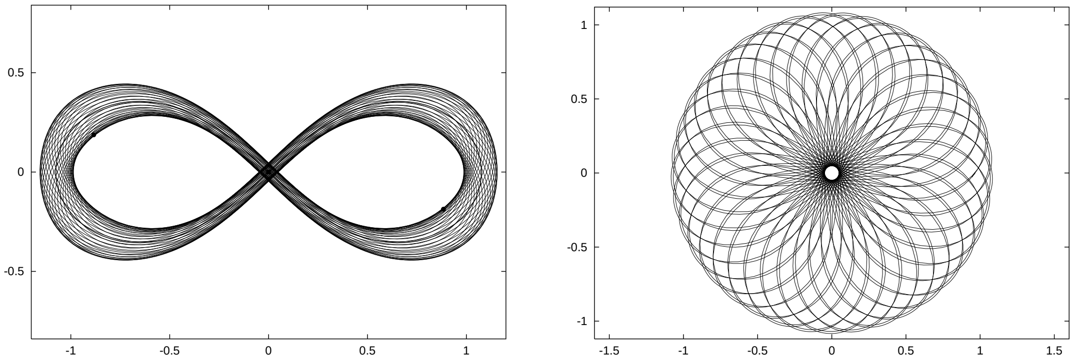

Figure 13: An example of a satellite choreography (left) and a relative choreography (right).

Another possibility is as follows. The eight has $c = 0$. it is possible to continue this periodic solution to values of $c \neq 0$, but to see it as a periodic solution we should use a rotating frame. I am indebted to M. Hénon who explored the continuation of the orbit with respect to angular momentum [4]. As he realized, the orbits obtained by continuation, in rotating frame, are again choreographies (see section 7). After one period in the rotating frame the orbit has rotated an angle δ in the fixed frame. By selecting δ to be a suitable rational multiple of 2π we can obtain a true choreography in a fixed frame. An example is shown in figure 13 right. The angle rotated when the orbit closes in the rotating frame is $\frac{3}{37}2\pi$.

7 Exploring for other absolute choreographies

Finally we pass to the search for other choreographies in a fixed frame.

The starting point is the continuation with respect to c. If along the family we return to fixed axes, we shall have another true or *absolute choreography* (as opposed to relative). As mentioned, the continuation is possible, but soon appears a binary collision in one of the orbits of the family. A characteristic curve of the family will be shown later. It is not difficult to continue the family beyond the orbit having a collision. Different devices can be used. The simplest one is to perform a Levi–Civita regularization every time we approach a binary collision. But another method will be presented later.

Proceeding along the family we find indeed another absolute choreography. After that the orbits of the family become more and more complicated, having several passages close to collision in one revolution (in rotating frame). No more absolute choreographies have been detected in this way.

A different approach to obtain relative choreographies and, in particular, absolute choreographies, is as follows. Consider initial conditions in isosceles configuration and with suitable velocities:

$$x_3 = x_2, \quad y_3 = -y_2, \quad \dot{x}_3 = -\dot{x}_2, \quad \dot{y}_3 = \dot{y}_2.$$

The conditions for m_1 are determined from the center of mass integrals. This isosceles triangle has a symmetry axis passing through m_1.

Assume that after some time τ the bodies pass through another isosceles configuration, this time with the body m_2 in the symmetry axis. Let β the angle between the previous symmetry axis (the x axis) and the present one. Assume that after rotating positions and velocities at time τ by an angle $-\beta$ we have an isosceles configuration *with the same symmetries concerning velocities than the initial one.* The only change is a circular permutation of the bodies with change of orientation. Then, is it immediate that the action of the semi-direct product of $\mathbb{Z}^2$ and $\mathbb{Z}^3$ (the symmetry and the permutation) produces a relative choreography with period $T = 6\tau$ and rotation angle 6β. In particular, if β is a multiple of π, we shall have an absolute choreography. It is clear that it will be symmetric with respect to the x axis.

To locate initial isosceles configurations and the related velocities (always on $h = -\frac{1}{2}$), we can proceed in different ways. One of them is to prescribe also c. Then we can have 0, 1 or 2 possible initial conditions, as intersection of an ellipse of given kinetic energy (eventually empty) with a line in the $(\dot{x}_2, \dot{y}_2)$ space. When proceeding along a family and using one of two roots, if a double root is found one has to shift to the other root. This occurs, for instance, on turning points of the characteristic family (e.g., in the space (c, T)). Another possibility is to choose a point on the ellipse of given kinetic energy by means of an auxiliary angle γ. So, the velocities will be of the form

$$\dot{x}_2 = \sqrt{3}\rho\cos(\gamma),\, \dot{y}_2 = \rho\sin(\gamma),$$

where ρ is the square root of the kinetic energy. Then the value of c can be obtained as $c = (6x_2\dot{y}_2 - 2y_2\dot{x}_2)/3$ (remember that the masses are equal and $\sum m_i = 1$). In order to have positive kinetic energy one should take (x_2, y_2) inside the *zero velocity curve, zvc,* defined by

$$\frac{1}{|y_2|} + \frac{4}{\sqrt{9x_2^2 + y_2^2}} = 1.$$

To any (x_2, y_2, γ) with (x_2, y_2) inside the zvc and $\gamma \in [0, 2\pi]$ corresponds an admissible isosceles configuration and related velocities. However, due to the symmetries, we can discard data with $x_2 < 0$, $y_2 > 0, c < 0$. Note that if a collision is produced at the initial time the angle γ has a jump discontinuity by π. No discontinuities occur along the family if the collision is produced at some $t > 0$.

Given values of (x_2, y_2, γ) one can start a numerical integration until a passage through an isosceles configuration is produced (with an arbitrary rotation). The integration has been stopped if $\tau > 5$ or an escape or too close approach to collision is produced. One could certainly look for successive passages through isosceles configuration, but using the first one has produced good enough results. Then a Newton procedure is started to fulfil the conditions on the velocities, by keeping γ fixed and allowing for changes in (x_2, y_2).

This procedure has been started on a grid of values of $\gamma \in [0, 2\pi]$ with step 1/4000. Different initial values of (x_2, y_2) inside the domain bounded by $x_2 = 0$, $y_2 = 0$, $x_2 = 1$ and the zvc with step 1/576 in x_2 and y_2 have been used. The process is stopped in case of escape or collision,

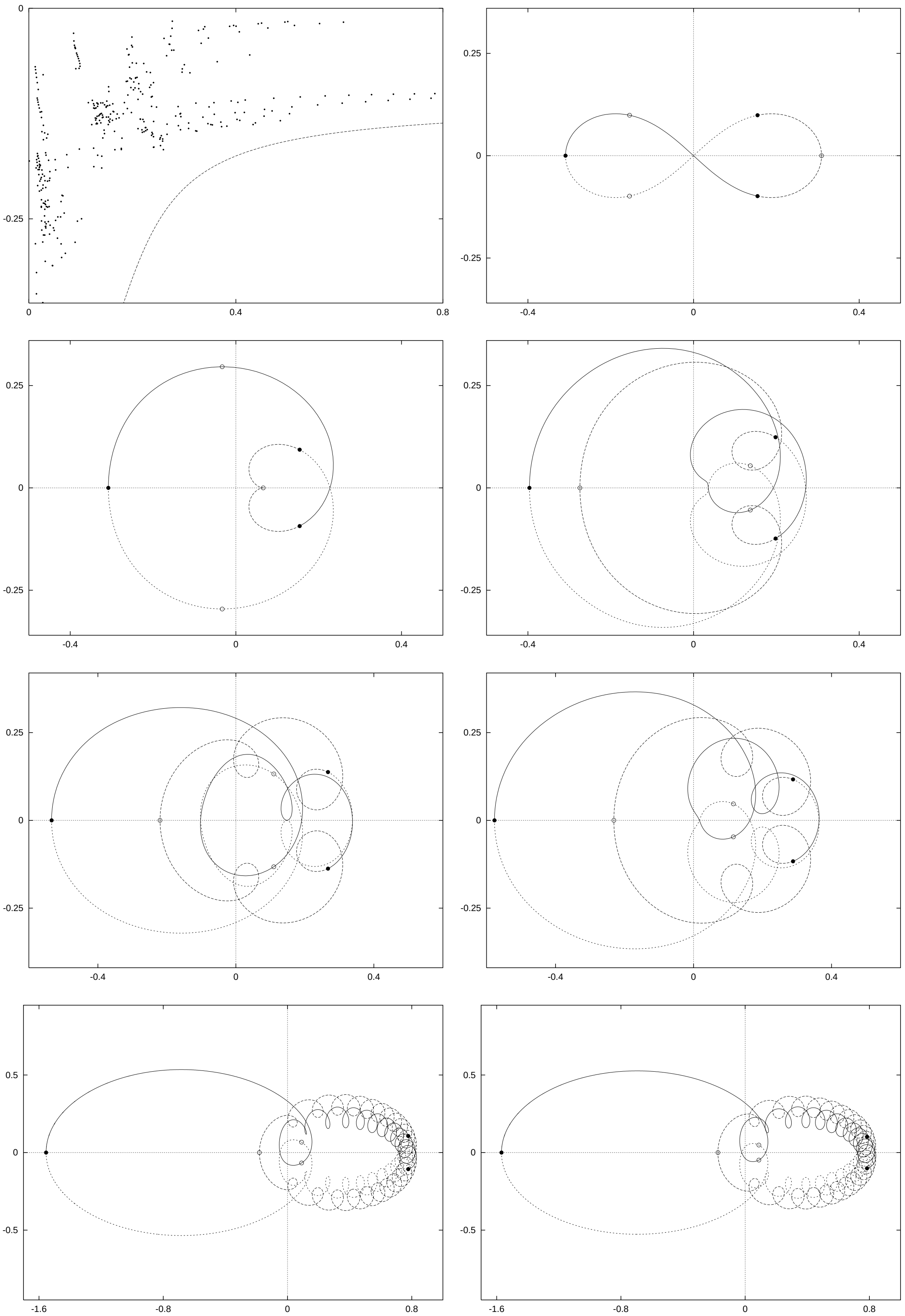

Figure 14: Top left: Locations of (x, y) for the initial isosceles configuration to obtain absolute choreographies. Top right: The figure eight. On the successive rows, more examples of absolute choreographies. See the text for additional explanations.

if the total period T becomes larger than 30, if the number of Newton iterates exceeds some bound, if the iterates move away from the admissible domain or if the method converges to a solution already found. In all near 1 billion initial conditions have been tested. From these near 3×10^5 relative choreographies have been found. At each one of them a continuation process is started. Of course many of them belong to the same continuation curve. Furthermore, when along a continuation curve one crosses a value $\beta = k\pi$, $k \in \mathbb{Z}$, the absolute choreography is refined.

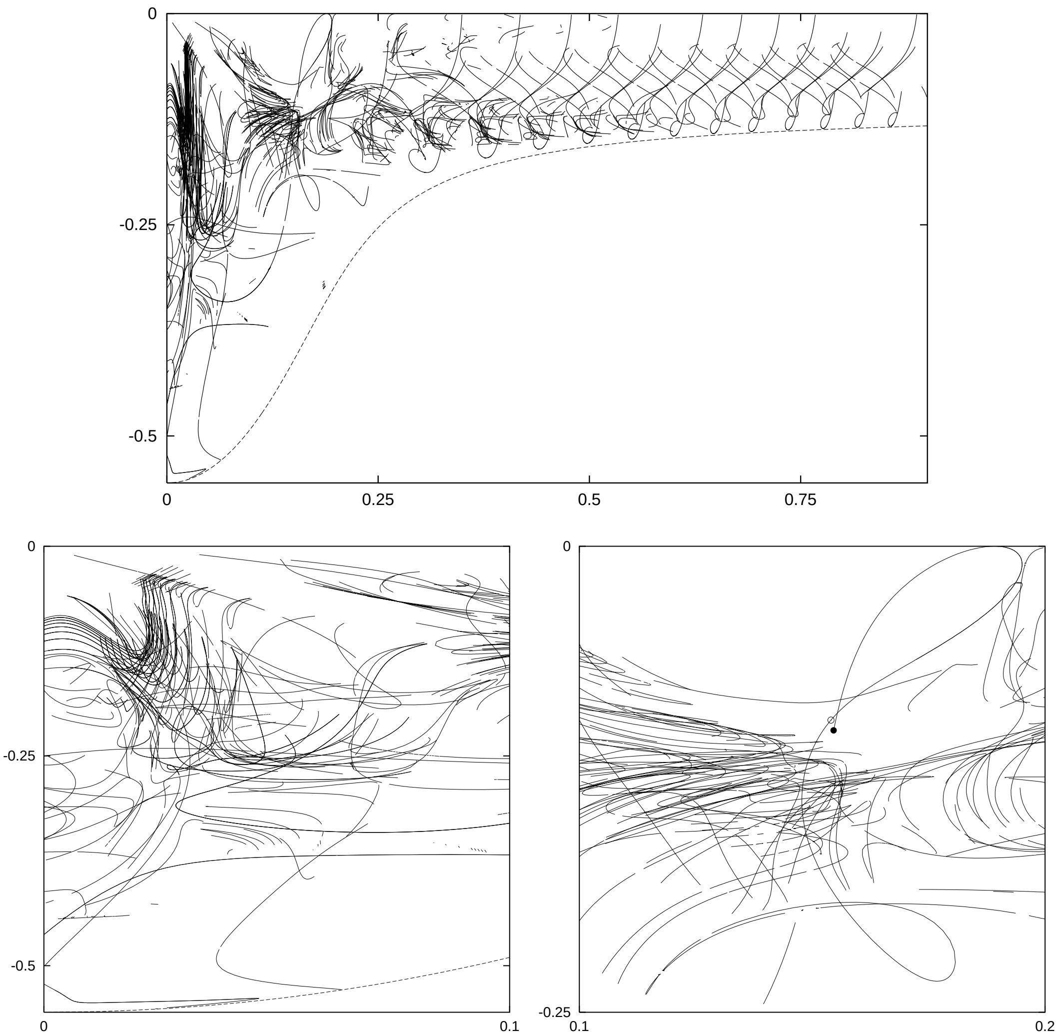

Figure 15: Characteristic curves of relative choreographies on the (x_2, y_2) plane. The zvc is shown as a dashed curve. On the bottom part some magnifications are shown. See the text for additional details.

Figures 14 and 15 show a sample of results. [1]. The top left plot of figure 14 shows values of (x_2, y_2) for which an absolute choreography has been found. Up to now (April 2001) 345 solutions of this type have been detected even limiting the period to 30 and skipping solutions passing too close to collision. Ordered by increasing period the first one is the eight. Points and circles along the orbit (and subsequent orbits), show the initial and final isosceles configurations used to obtain the solution. The second row of the figure shows next choreography with the lowest

[1] Files containing the data to display the choreographies found, running `gnuplot` under `linux` or `unix`, are available at `http://www.maia.ub.es/dsg`.

period and another one, also with low period. The one on the left belongs to the continuation curve of the eight. The third row displays choreographies numbers 6 and 7 by increasing period. It is interesting to see that by increasing the number of revolutions on the binary part of the orbit (mainly on $x > 0$ in the plots), one obtains two countable sets of absolute choreographies. In them the center of masses of a binary and a third body move close to elliptic orbits until an exchange is produced. Last row in figure 14 shows the last member of both families with $T < 30$. The corresponding points on the top left plot appear as a sequence relatively close to the zvc to the right. But many other families are present. The choreographies in the last row belong to the simplest families. Note also that some families of absolute choreographies are symmetric both with respect to the x and y axes.

Approximate values of initial conditions and 1/6 of the period for the orbits in rows 2 to 4 in figure 14 are given below. Except on the figure eight solution, the angular momentum on these solutions is greater than 0.19. In fact, all the 345 choreographies found, have angular momentum greater than 0.12, except the eight.

row		γ	x_2	y_2	τ
2	left	0.73976160	0.15402894	−0.09324743	0.44929802
2	right	0.80535382	0.19818361	−0.12376832	1.08886765
3	left	0.70450055	0.26707603	−0.13756835	1.43912861
3	right	0.60277109	0.28844514	−0.11671861	1.45630457
4	left	0.29968793	0.77718110	−0.10676744	4.72345735
4	right	0.26175926	0.78447812	−0.10133157	4.72368628

Figure 15 shows, on the top, characteristic curves of relative choreographies on the (x_2, y_2) variables. A simple structure is repeated on the upper right part, between the zvc and $y = 0$. It is clear that these structures repeat indefinitely, with increasing periods. To the left of this plot the situation becomes cumbersome. Suitable magnifications are shown on the bottom. For $x_2 \in [0.0, 0.1]$ several families can also be guessed. For $x_2 \in [0.1, 0.2]$ there is a distinguished family, starting at the marked point, which corresponds to the figure eight. Proceeding along the family one reaches $y_2 = 0$, at which the collision is produced. Later on the characteristic curve passes through a point marked with a small circle (very close to the initial point of the figure eight solution in this projection). This new marked point corresponds to the absolute choreography on the second row, left, in figure 14. Continuing along the family some interruptions can be seen. They are related to passages too close to collision.

No one of the absolute choreographies found up to now is stable beyond the figure eight.

Acknowledgements

This work has as starting point the discussions and suggestions made by A. Chenciner and R. Montgomery. With the exception of the last section, most of the work was done during a sabbatical leave at the Institut de Mécanique Celeste (Observatoire de Paris), thanks to the support of CNRS. My gratitude to the colleagues at that institution for the hospitality and interest on the work. The parallel computing facilities of the UB Grup de Sistemes Dinàmics have been widely used. The support of grants BFM2000–805 (Spain) and 2000SGR–27 (Catalonia) is also acknowledged.

References

[1] A. Chenciner. Action minimizing periodic orbits in the Newtonian n–body problem, these *Proceedings*.

[2] A. Chenciner and R. Montgomery. A remarkable periodic solution of the three body problem in the case of equal masses, *Annals of Mathematics*, **152**, 881–901 (2000).

[3] A. Chenciner, J. Gerver, R. Montgomery and C. Simó. Simple choreographic motions of N bodies with strong forces, to appear in *Geometry, Mechanics, and Dynamics*, Springer.

[4] M. Hénon, private communication (2000).

[5] R. Montgomery. Action spectrum and Collisions in the three–body problem, these *Proceedings.*

[6] C. Moore. Braids in Classical Gravity, Physical Review Letters **70**, 3675–3679 (1993).

[7] C. Simó. Analytical and numerical computation of invariant manifolds, in *Modern Methods in Celestial Mechanics*, ed. D. Benest and C. Froeschlé 285–330, Paris, Editions Frontières, 1990.

[8] C. Simó. Effective Computations in Hamiltonian Dynamics, in *Cent ans après les Méthodes Nouvelles de H. Poincaré*, Paris, Société Mathématique de France, 1–23, 1996.

[9] C. Simó. New families of Solutions in N–Body Problems, to appear in *Proceedings of the ECM 2000*, Barcelona (July, 10–14). Available at `http://www.iec.es/3ecm`.

[10] C. Simó. Periodic orbits of the planar N–body problem with equal masses and all bodies on the same path, to appear in *The Restless Universe: Applications of N-Body Gravitational Dynamics to Planetary, Stellar and Galactic Systems*, ed. B. Steves, Bristol, IOP Publishing, 2001.

[11] C. Simó. Global Dynamics and Fast Indicators, to appear in *Global Analysis of Dynamical Systems*, ed. H. W. Broer, B. Krauskopf and G. Vegter, Bristol, IOP Publishing, 2001.

[12] J. Stoer and R. Bulirsch. *Introduction to Numerical Analysis*, Springer-Verlag, 1983 (second printing).